Check for updates

Reusable isotype heterojunction g-C₃N₄/alginate hydrogel spheres for photocatalytic wastewater treatment†

Yuito Narita,[a] Kento Nishi,[b] Tatsushi Matsuyama[b] and Junichi Ida ⓘ *[b]

Various visible-light-driven photocatalysts have been studied for practical applications in photocatalytic wastewater treatment *via* solar irradiation. Among them, g-C₃N₄ has attractive features, including its metal-free and environmentally friendly nature; however, it is prone to charge recombination and has low photocatalytic activity. To solve these problems, isotype heterojunction g-C₃N₄ was recently developed; however, the methods employed for synthesis suffered from limited reproducibility and efficiency. In this study, isotype heterojunction g-C₃N₄ was synthesized from various combinations of precursor materials using a planetary ball mill. The isotype heterojunction g-C₃N₄ synthesized from urea and thiourea showed the highest photocatalytic activity and completely decolorized Rhodamine B (RhB; 10 ppm) in 15 min under visible-light irradiation. Furthermore, to improve recyclability, isotype heterojunction g-C₃N₄ was immobilized in alginate hydrogel spheres. The isotype heterojunction g-C₃N₄/alginate hydrogel beads were used in 10 repeated RhB degradation experiments and were able to maintain their initial photocatalytic activity and mechanical strength. These achievements represent an advance towards practical, sustainable photocatalytic wastewater treatment.

1. Introduction

Sustainable, sunlight-powered photocatalytic wastewater treatment technologies have undergone considerable recent development. However, their photocatalytic efficiencies and device lifetimes remain insufficient for practical applications. TiO₂ has been thoroughly studied as a typical photocatalyst because of its strong photocatalytic activity under UV irradiation. TiO₂ features band gaps for its anatase (3.2 eV) or rutile (3.0 eV) polymorphs that require UV irradiation (λ < 380 nm) for photoexcitation;[1] however, UV radiation comprises a relatively low proportion (4%) of solar radiation.[2] Extensive efforts to tune TiO₂ band gaps *via* incorporation of additives have been reported. Anionic dopants, such as nitrogen and sulfur,[3,4] grafted metal cations that induce interfacial charge transfer, such as Cu(II), Ce(III), and Fe(III),[5–7] and dye sensitizers[8,9] each bear various disadvantages. Alternative semiconductors with narrow band gaps may offer simpler routes to improved photocatalysts.[10–12]

Notably, undoped graphitic carbon nitride (g-C₃N₄) semiconductors have an appropriate band gap range (2.6–2.8 eV)[13–16] for efficient solar photocatalysis. g-C₃N₄ is synthetically accessible from various solvent-free reactions of inexpensive precursors; furthermore, g-C₃N₄ is metal-free, non-toxic, chemically/thermally stable and environmentally benign. However, g-C₃N₄ device architectures must be designed to suppress otherwise rapid electron–hole recombination. Fortunately, heterojunction device designs may improve charge separation.[17–19] In a typical charge transfer pathway through a heterojunction (Type II), excited electrons move to a semiconductor with a relatively lower conduction band, whereas holes move to another semiconductor with a higher valence band, thus enhancing charge separation.[20] Previous efforts to produce g-C₃N₄ heterojunctions have involved the complex, prolonged, and wasteful synthesis of composites that include metal oxides. More recent reports describe one-step synthetic routes to g-C₃N₄ heterojunction compositions that exclude metal oxides. Solehudin *et al.* and Liao *et al.* synthesized isotype heterojunction g-C₃N₄ by calcining a mortar-crushed mixture of urea and melamine;[21,22] however, manual mixing methods are challenging to reproduce. Balakrishnan *et al.* developed citric acid-assisted chemically functionalized black g-C₃N₄ isotype heterojunction hydrogels for tetracycline degradation and H₂O₂ production and demonstrated excellent photocatalytic decomposition performance for tetracycline degradation.[23] Dong *et al.* reported isotype heterojunction g-C₃N₄ by calcining precursors deposited from a dried solution of urea and thiourea;[24]

[a]Environmental Engineering for Symbiosis, Graduate School of Science and Engineering, Soka University, 1-236 Tangi-cho, Hachioji-shi, Tokyo 192-8577, Japan

[b]Department of Science and Engineering for Sustainable Innovation, Faculty of Science and Engineering, Soka University, 1-236 Tangi-cho, Hachioji-shi, Tokyo 192-8577, Japan. E-mail: ida@soka.ac.jp

unfortunately, solvent requirements restrict mass producibility in this case. Further investigation is required to elucidate the relationship between precursor composition and photocatalytic activity of isotype heterojunction g-C$_3$N$_4$. Balakrishnan *et al.* also developed phosphorylated g-C$_3$N$_4$/sulfur-self-doped- g-C$_3$N$_4$ homojunction carboxymethyl cellulose beads for highly efficient photocatalytic generation of H$_2$O$_2$ under visible light.[25] The homo-junction g-C$_3$N$_4$ is characterized by a simple manufacturing process due to the use of the same material, high thermal and chemical stability for long-term use, and limited charge carrier separation efficiency compared to hetero-junctions, leading to less effective recombination suppression. Therefore, we focused on isotype heterojunction g-C$_3$N$_4$ in this study.

For practical applications, photocatalysts must be sufficiently reusable; however, device designs have required trade-offs between reusability and performance. Increased photocatalyst surface area facilitates efficient contact with the degradation target, leading to increased photocatalytic reaction rates. Accordingly, recent reports have identified photocatalysts with high specific surface area nanostructures.[11,26,27] Unfortunately, such photocatalyst particles have lower compatibility with solid–liquid separation methods, diminishing reusability and foreshadowing environmental nanopollution.[28] Photocatalysts may be recovered using laboratory-scale centrifugation; however, wastewater treatment facilities are not equipped for continuous centrifugation processes. Reassuringly, photocatalyst immobilization techniques may improve high surface area photocatalyst recovery.

Alginate is a natural, biodegradable and environmentally benign polysaccharide extractable from brown algae. Alginate materials have been applied as food additives,[29] drug delivery carriers,[30] dye or heavy metal ion adsorbents,[31] and polymer flocculant.[32,33] Alginate polymers consist of various proportions and distributions of 1,4-linked β-D-mannuronic acid and α-L-guluronic acid. Alginate carboxyl groups interact electrostatically with multivalent cations to instantaneously form hydrogels, which have been applied to immobilize biocatalysts or enzymes. Alginate biocatalyst immobilization has been demonstrated using two approaches that impart different macrostructures. Alginate beads may be formed by addition of a catalyst-containing alginate solution a crosslinker.[33] Alginate capsules with a hard outer shell and viscous core were synthesized *via* addition of a viscous solution containing the cross-linker and catalyst into an alginate solution.[34] By encapsulating g-C$_3$N$_4$ in hydrogel beads or capsule, the operability of g-C$_3$N$_4$ in practical and large-scale applications is improved and possible nanopollution is prevented, increasing the potential for commercialization.[25,35] Although two such cases of g-C$_3$N$_4$ immobilization in alginate beads and capsules have been reported, their photocatalytic activities are low and further improvement is required to apply for practical application.[36,37]

We hypothesized that reproducible g-C$_3$N$_4$ heterojunctions could be practically synthesized, immobilized in alginate, and applied as durable and efficient photocatalysts. We first combined various sets of solid precursor materials using planetary ball milling to form g-C$_3$N$_4$ heterojunctions. We then evaluated their photophysical properties using X-ray diffraction (XRD), Fourier-transform infrared spectroscopy (FT-IR), and UV-vis diffuse reflectance spectroscopy. Additional properties, such as Brunauer–Emmett–Teller (BET) specific surface area, hydrodynamic diameter, and zeta potential, were also evaluated. Then, we evaluated their visible light-powered photocatalytic activity for the degradation of Rhodamine B (RhB). We then evaluated the activity and durability of solid bead or hollow capsule photocatalysts containing alginate hydrogel sphere-immobilized g-C$_3$N$_4$.

2. Material and methods

2.1. Materials

The following reagents were purchased from commercial sources and used without further purification. Guaranteed reagent-grade urea, thiourea, calcium chloride anhydrate (CaCl$_2$), and ammonium oxalate monohydrate (AO); Wako special-grade melamine and *p*-benzoquinone (BQ); and Wako 1st-grade sodium alginate (80–120 cP; 10 g L^{-1}, 20 °C) were purchased from FUJIFILM Wako Pure Chemical (Osaka, Japan). Polyvinylpyrrolidone (PVP; Ave. M.W. 1 300 000) was purchased from Sigma-Aldrich (St. Louis, MO, USA). Chemical usage-grade rhodamine B was purchased from JUNSEI CHEMICAL (Tokyo, Japan). Aeroxide® P25 was purchased from Evonic Industries AG (Essen, NRW, Germany). Liquid chromatography-grade 2-propanol (IPA) was purchased from Merck KGaA (Darmstadt, HE, Germany).

2.2. Synthesis of g-C$_3$N$_4$

Isotype heterojunction g-C$_3$N$_4$ was synthesized by a modified literature procedure.[21,24] In a representative synthetic procedure, urea and thiourea (1 : 1 by wt.) were placed in a zirconia bowl (45 mL) with zirconia balls (15 mm × 7) and mixed using a planetary ball mill (Pulverisette 7 Classic Line, Fritsch, Idar-Oberstein, RP, Germany; 15 min; 300 rpm). The obtained powder was transferred to an alumina crucible with a lid and heated under air (5 °C min^{-1}) to the desired calcination temperature (550 °C; 2 h). The resultant g-C$_3$N$_4$ sample (CN-TU) was cooled (25 °C) and collected. Analogous syntheses using melamine and urea are denoted as CN-MU. Non-heterojunction g-C$_3$N$_4$ samples were synthesized separately from single components (urea, CN-U; thiourea, CN-T; and melamine, CN-M).

2.3. Synthesis of g-C$_3$N$_4$/Alg beads

CN-TU (1% w/v) was added to ultrapure water and sonicated (400 W, 20 kHz, 30 min). Then, sodium alginate (1% w/v) was added, and the resultant heterogeneous mixture was vigorously stirred and placed in a syringe with a 26G (0.23 mm i.d.) needle. Using a syringe pump, the mixture was added dropwise into a stirring (500 rpm; 20 min) aqueous solution of CaCl$_2$ (0.1 M), after which the beads were fully crosslinked. Finally, the obtained g-C$_3$N$_4$/Alg beads were recovered by straining through a colander and washed by stirring in ultrapure water (30 min).

2.4. Synthesis of g-C₃N₄/Alg capsules

CN-TU (2% w/v) was sonicated in aqueous in CaCl₂ (0.5 M) (30 min). PVP (8% w/v) was then added as a thickening agent and dissolved *via* vigorous stirring. Using a syringe pump, the resultant heterogeneous mixture was placed in a syringe with a 26G needle and added dropwise to a stirring (700 rpm; 5 min) aqueous solution of sodium alginate (0.5% w/v), after which the capsules were fully crosslinked. Finally, the obtained g-C₃N₄/Alg capsules were recovered by straining through a colander and washed by stirring in ultrapure water (30 min).

2.5. Characterization of g-C₃N₄

The phase structures of the powder samples were analyzed by XRD using a Bruker D8 ADVANCE diffractometer (Billerica, MA, USA) with a Cu Kα ($\lambda = 1.5418$ Å) radiation source (40 kV; 40 mA). Diffraction patterns were obtained over a scan range ($2\theta = 10°$–60°; step width, 0.1°; scan rate, 0.5° s^{-1}). Sample chemical compositions were identified by FT-IR using a Shimadzu (Kyoto, Japan) IRAffinity-1S spectrophotometer (resolution, 1 cm^{-1}; cumulative number, 20). The samples were prepared as KBr tablets. Diffuse reflection spectra of the samples were measured using a JASCO (Tokyo, Japan) V-650 UV-vis spectrometer equipped with an integrating sphere. BaSO₄ was used as the standard. Tauc plots were analyzed to obtain sample band gaps. The photoluminescence spectra were measured using a Shimazu (Tokyo, Japan) RF-5300PC spectrofluorophotometer to assess the recombination of the photo-generated holes and electrons of the different samples.

Nitrogen adsorption–desorption isotherms (−196 °C) were measured using a Micromeritics (Norcross, GA, USA) ASAP 2020 after sample degassing (250 °C; 3 h). The specific surface areas of the samples were analyzed using the BET multi-point method. Sample hydrodynamic diameters were measured by dynamic light scattering (DLS) using a Beckman Coulter (Brea, CA, USA) DelsaMax Pro. Simultaneously, sample electrophoretic mobilities in ultrapure water were measured, and the zeta potential was determined based on the following Smoluchowski (eqn (1)):

$$v = \varepsilon \zeta E / \mu \qquad (1)$$

where v is the electrophoretic mobility, ε is the dielectric constant of the solvent, ζ is the zeta potential, E is the electric field, and μ is the viscosity of the solvent.

2.6. Photocatalytic degradation experiments

The photocatalytic activity of the samples was evaluated based on the visible-light degradation of RhB. To achieve adsorption equilibrium between the photocatalyst and the degradation targets, the photocatalytic sample was added to aqueous RhB (10 ppm) and stirred (30 min) in the dark. Equivalent masses (0.1 g) of the as-prepared g-C₃N₄ powder (0.1 g), g-C₃N₄/Alg bead (1000 pieces), or g-C₃N₄/Alg capsule (500 pieces) photocatalysts were added. The samples were irradiated with visible light ($\lambda > 440$ nm) using a USHIO (Tokyo, Japan) UXR-300BF xenon lamp (300 W) equipped with a UV cut-off filter. The RhB

concentration was monitored by measuring the absorbance ($\lambda = 553$ nm) using a JASCO V-650 UV-vis spectrophotometer and plotted as the normalized concentration c_t/c_0 [%]. For powder samples, particles were removed by centrifugation (13 000 rpm; 30 min) prior to absorbance measurements. To evaluate photocatalytic activity, pseudo-first-order reaction rate constants were calculated using eqn (2):

$$-\ln(c_t/c_0) = kt \qquad (2)$$

where c_t is the RhB concentration at irradiation time t, c_0 is the initial concentration of RhB, and k is the rate constant.

2.7. Active species trapping experiments

Active species trapping experiments were conducted to identify the active species contributing to RhB degradation. IPA, BQ, and AO (7.5 mM) were used as scavengers for $^{\bullet}$OH, $^{\bullet}$O$_2^{-}$, and the holes, respectively. These experiments were carried out using the same procedure as in Section 2.6, except for the addition of scavengers.

2.8. Recycling tests of g-C₃N₄/Alg beads

To evaluate the durability of recycled g-C₃N₄/Alg beads, RhB degradation experiments described in section 2.6 were repeated 10 times, with an additional bead washings step in between each cycle involving stirring (30 min) the beads in ultrapure water to remove residual adsorbed RhB. Scanning electron microscopy (FE-SEM) using a JEOL (Tokyo, Japan) JSM-7500M microscope (acceleration voltage, 5 kV; emission current, 10 μA) imaged the g-C₃N₄/Alg bead surfaces before and after the tests. Microscopy samples were vacuum freeze-dried and sputter-coated with osmium, an antistatic agent. In addition, the compressive strength of the beads was measured using an A&D (Tokyo, Japan) STB-1225S universal testing machine equipped with a load cell (50 N). The elastic modulus was determined based on the data within 0–20% of the strain range by using the following Hertz model (eqn (3)):

$$F = 4/3ED^{0.5}\Delta D^{1.5} \qquad (3)$$

where F is the load, E is the modulus of elasticity, D is the bead diameter, and ΔD is the displacement.

3. Results and discussion

3.1. Characterization

Fig. 1 shows similar XRD patterns for each sample. A stronger high angle signal (27.4°, 002) is attributable to the interlayer stacking of the aromatic units of g-C₃N₄, whereas the smaller low angle signal (13.3°, 002) to the repetition of the triazine units in the plane.[38] These data are consistent with successful syntheses of g-C₃N₄ using each set of conditions. In addition, CN-U and CN-T exhibited smaller and broader peaks than CN-M, indicative of their lower crystallinity. Plausibly, their urea and thiourea precursor materials, which are known to generate various intermediates in the calcination process, disrupted the formation of uniform and well-connected heptazine-based g-
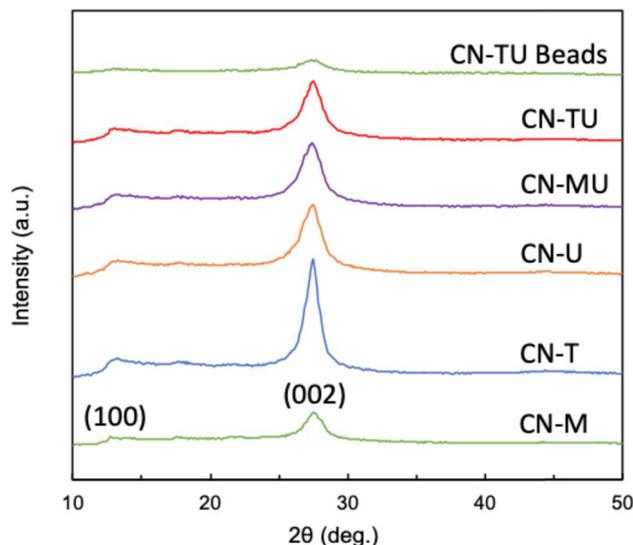
Fig. 1 X-ray diffraction patterns of g-C_3N_4 synthesized from different raw materials.

C_3N_4.[39] In contrast, melamine contains a triazine subunit, which could promote polymerization, leading to the relatively higher crystallinity for CN-M. The result of XRD spectra for CN-TU encapsulated in alginate is also shown in Fig. 1. Although peak intensity is low, the peaks at 27.4° and 13.3° indicate the successful formation of g-C_3N_4/Alg beads.

Fig. 2 shows similar FTIR spectra for each sample; material differences for each type of g-C_3N_4 did not impart spectral differences. Furthermore, the spectral data are typical for g-C_3N_4, suggesting successful syntheses. The sharpest peak (800 cm^{-1}) was attributed to the breathing vibration of the triazine unit.[21–24,38] Two peaks (1200–1350 cm^{-1}) are attributed to the out-of-plane bending vibration of the heteroaromatic ring.[40] Multiple peaks (1400–1700 cm^{-1}) are attributed to the
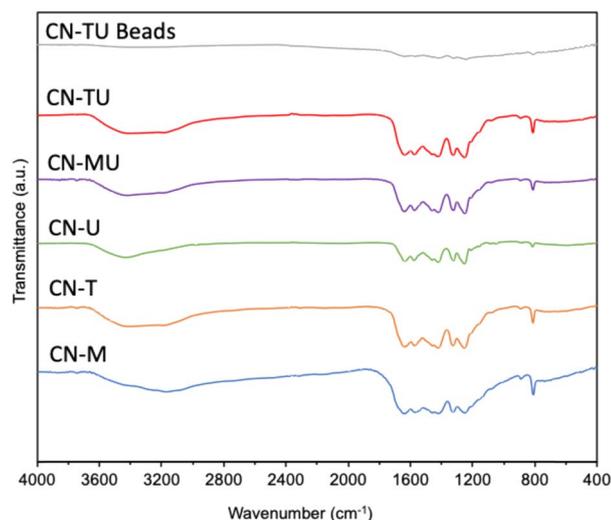
C=N stretching vibration of the heteroaromatic ring.[22] A broad peak (3000–3650 cm^{-1}) is attributed to N–H and O–H stretching vibrations, suggesting the presence of uncondensed amine groups and adsorbed water molecules on the particle surface.[24,40] In addition, no unique peaks were observed for CN-TU and CN-T synthesized from raw materials containing sulfur atoms, suggesting that sulfur was desorbed as SO$_X$ during calcination. The result of FTIR spectra for CN-TU encapsulated in alginate is also shown in Fig. 2. Despite low absorption due to the dilution of g-C_3N_4 by alginate, successful encapsulation of g-C_3N_4 in alginate is confirmed.

Fig. 3 shows the UV-vis diffuse reflectance spectra of each sample. As shown in Table S.1†, the band gaps of each sample are varied but within the visible range. The absorption edges of all samples (450–480 nm) are appropriate for high reactivity under visible-light irradiation. Zhang et al. reported that they successfully improved the visible-light absorption of g-C_3N_4 by adding different amounts of barbituric acid (BA) to the raw dicyandiamide material.[41] In their study, the C/N ratio of g-C_3N_4 increased with increasing BA content, narrowing the band gap. Therefore, differences in C/N ratio, plausibly originating from differences in precursor materials, may be responsible for the varied band gaps of the g-C_3N_4 samples. For the samples obtained from blends of two precursor materials, the band gap of CN-TU was located between those of CN-T and CN-U, and CN-MU, between CN-M and CN-U. The optical properties of the prepared g-C_3N_4 are consistent with previous reports,[21,24] suggesting the formation of isotype heterojunctions in CN-TU and CN-MU.

The photoluminescence (PL) spectra of the samples were analyzed to examine the recombination of the photo-generated holes and electrons and the results are shown in Fig. 4.[23] The g-C_3N_4 samples prepared using a single starting material such as CN-T, CN-U, and CN-M show higher intensity meaning higher recombination. In contrast, the g-C_3N_4 samples prepared using two starting materials such as CN-TU and CN-MU show
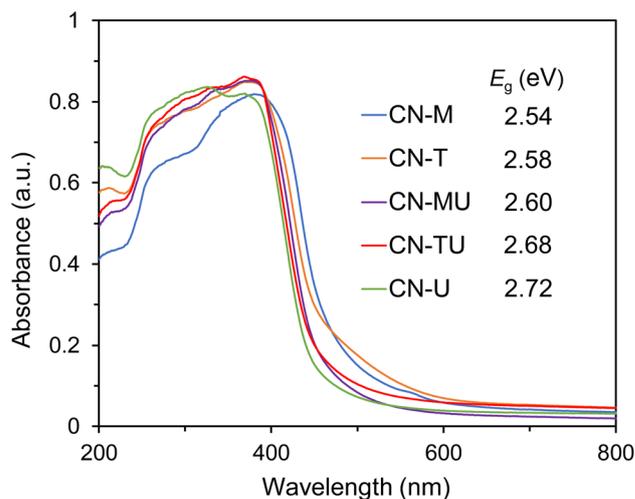

Fig. 2 FT-IR spectra of g-C_3N_4 synthesized from different raw materials.

Fig. 3 UV-vis diffuse reflectance spectra and band gap energies of g-C_3N_4 synthesized from different raw materials.

View Article Online

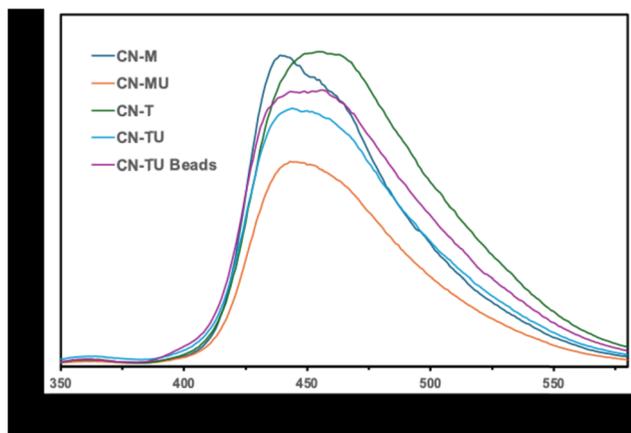**RSC Advances**

Paper

Open Access Article. Published on 02 July 2024. Downloaded on 4/28/2026 11:28:20 PM. This article is licensed under a Creative Commons Attribution-NonCommercial 3.0 Unported Licence.

Fig. 4 Photoluminescence (PL) of g-C_3N_4 synthesized from different raw materials.

Fig. 5 RhB degradation by g-C_3N_4 synthesized from different raw materials under visible light irradiation.

relatively lower intensity meaning suppressed recombination. The results also support the formation of hetero type.

Table S1† shows significant differences in BET specific surface areas for each set of precursor materials. Urea and thiourea precursors, which release soft bubbles of NH_3, H_2S, and CO_2 gases during the polymerization process, produced more porous g-C_3N_4.[42] Moreover, the relatively small particle size (hydrodynamic diameter) of CN-U suggests that urea generates g-C_3N_4 with a lower degree of polymerization.

The surface charge of photocatalytic particles affects the adsorption properties of the degradation targets. The isoelectric point of g-C_3N_4 has been reported to be between pH 4.4–5.1, with a negative zeta potential at higher pH.[40,43] Table S1† shows zeta potentials in ultrapure water that are consistent with previous reports and suggest that g-C_3N_4 selectively absorbs cationic compounds.

3.2. Photocatalytic performance of g-C_3N_4

Photocatalytic degradation experiments were performed under visible-light irradiation using RhB (10 ppm) as a representative pollutant, and compared against P25, the best-known commercial TiO_2 photocatalyst. Fig. 5 shows the temporal changes in the RhB concentration; the gray area represents the time period prior to visible-light irradiation whilst RhB was adsorbed on the photocatalyst surface in the dark. The RhB concentration decreased during dark period before the beginning of irradiation ($t = 0$), indicating that g-C_3N_4 is highly adsorptive for RhB. The high adsorptivity may originate from electrostatic interactions between the negatively charged g-C_3N_4 surface and the RhB cationic dye. Furthermore, all g-C_3N_4 samples showed higher activity than P25. The CN-TU-forming isotype heterojunction exhibited the highest photocatalytic activity and completely decolorized RhB in 15 min.

Fig. 6 shows the relationship between sample BET specific surface area and photocatalytic activity. The photocatalytic activities of non-heterojunction CN-U, CN-T, and CN-M were proportional with BET specific surface area. The plots for CN-TU and CN-MU, which were formed with isotype heterojunctions,
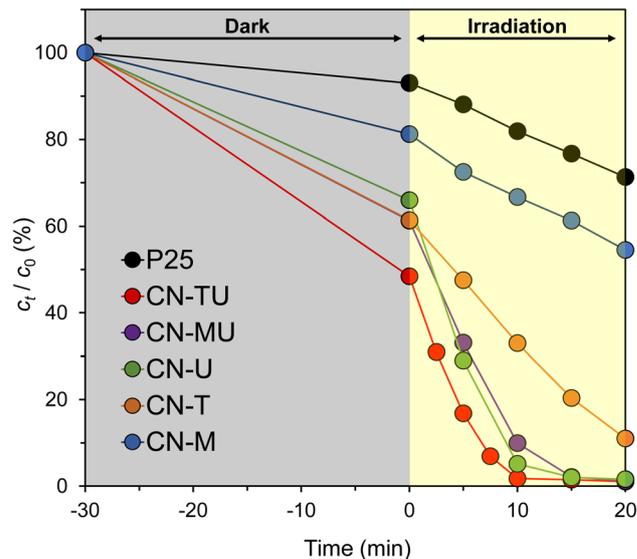
were higher than would be predicted by the linear relationship for the non-heterojunction samples. Plausibly, these samples featured isotype heterojunctions that improved charge separation, offering improved activity beyond what their surface areas could offer otherwise. CN-MU showed lower photocatalytic activity than CN-U, possibly because the negative effect of the low specific surface area derived from melamine exceeded the positive effect of improved charge separation. These data suggest that urea and thiourea are the optimal precursor materials for the synthesis of isotype heterojunction g-C_3N_4 with large surface areas.
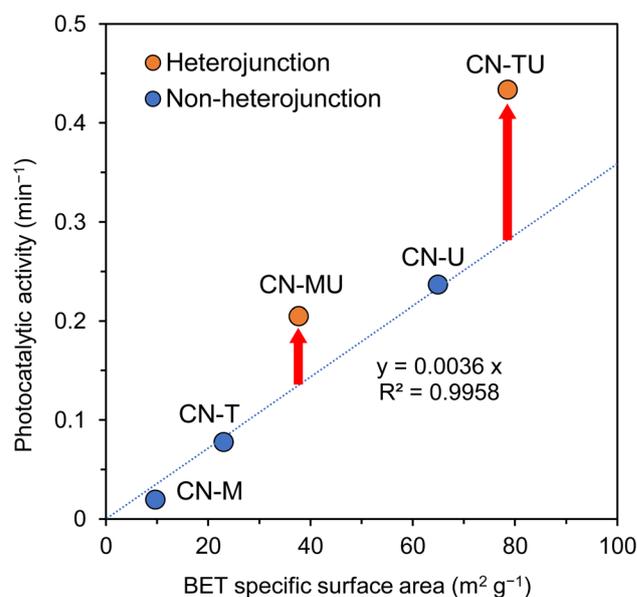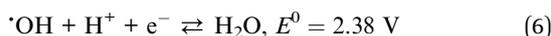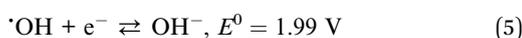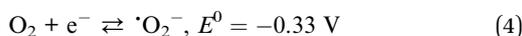

Fig. 6 Relationship between BET specific surface area and photocatalytic activities.

3.3. Active species trapping experiments

To identify the active species generated by g-C$_3$N$_4$, active species trapping experiments were performed using CN-TU and appropriate scavengers. Fig. 7 shows BQ, a $^{\cdot}O_2^-$ scavenger, inhibited the degradation reaction to the greatest extent. AO, a hole scavenger, offered slightly decreased inhibition, whereas IPA, an $^{\cdot}OH$ scavenger, provided minimal inhibition. These data suggest that $^{\cdot}O_2^-$ and h$^+$ are involved in RhB degradation by CN-TU. Dong *et al.* reported that isotype heterojunction g-C$_3$N$_4$ synthesized from urea and thiourea had a valence band and conduction band levels of 1.76 and −0.82 eV, respectively.[24] Eqn (4) describes the generation of $^{\cdot}O_2^-$ by the reduction of oxygen, whereas eqn (5) and (6) describe the generation of $^{\cdot}OH$ by the oxidation of OH$^-$ and H$_2$O, respectively.

$$O_2 + e^- \rightleftarrows {}^{\cdot}O_2^-, \; E^0 = -0.33 \text{ V} \tag{4}$$

$$^{\cdot}OH + e^- \rightleftarrows OH^-, \; E^0 = 1.99 \text{ V} \tag{5}$$

$$^{\cdot}OH + H^+ + e^- \rightleftarrows H_2O, \; E^0 = 2.38 \text{ V} \tag{6}$$

Therefore, CN-TU has sufficient reduction potential to generate $^{\cdot}O_2^-$, but insufficient oxidation potential to generate $^{\cdot}OH$. Plausibly, $^{\cdot}O_2^-$ generated by the reduction of dissolved oxygen by excited electrons or direct oxidation by holes is the source of RhB degradation.

3.4. Photocatalytic performance of g-C$_3$N$_4$/Alginate hydrogel spheres

We attempted to improve the recovery and reusability of CN-TU, which had the highest photocatalytic activity in powder form, by immobilizing it in alginate hydrogel spherical capsules or beads. These hydrogel spheres are composed of environmentally benign natural polysaccharides and calcium ions. Alginate hydrogel spheres were synthesized by one-step methods yielding g-C$_3$N$_4$/Alg beads or hollow g-C$_3$N$_4$/Alg capsules. The microscopic images in Fig. 8 reveal that relative to the transparent alginate beads (Fig. 8a), g-C$_3$N$_4$/Alg beads (Fig. 8b) contained uniformly dispersed g-C$_3$N$_4$ throughout the hydrogel. For the g-C$_3$N$_4$/Alg capsules (Fig. 8c), g-C$_3$N$_4$ was encapsulated in the core surrounded by an alginate shell. The diameters of the g-C$_3$N$_4$/Alg beads and g-C$_3$N$_4$/Alg capsules were 2.43 ± 0.10 and 4.42 ± 0.06 mm, respectively. The thickness of the alginate shell in the g-C$_3$N$_4$/Alg capsules was 0.33 ± 0.08 mm. In the capsules, Ca^{2+} in the droplets cross-linked the alginate while diffusing outward from the droplet owing to the concentration gradient. In contrast, in the case of beads, cross-linking occurs by Ca^{2+} entering into alginate droplets from the outer surface to the inside. Consequently, the diameter of the capsules was larger than that of the beads despite using the same injection needle. These hydrogel spheres were well-dispersed in stirring water and immediately settled when the stirring was halted.

To discuss recovery of photocatalyst in more detail, we compared the terminal settling velocity of g-C$_3$N$_4$/Alg beads and powdered g-C$_3$N$_4$ in water. The former was determined by measuring the actual time taken for the beads to settle for a fixed depth, while the latter was calculated from the median diameter of CN-TU (1.2 μm, Table S1†) by using the following Stokes' (eqn (7)):

$$v_s = g(\rho_p - \rho_f)d_p^2/18\eta \tag{7}$$

where v_s is the terminal settling velocity, g is the gravitational acceleration, ρ_p is the density of the particles, ρ_f is the density of water, d_p is the particle size, and η is the viscosity of water. As a result, the terminal settling velocity of g-C$_3$N$_4$/Alg beads was measured to be 1.36 cm s^{-1}, while that of powdered g-C$_3$N$_4$ was calculated to be 0.11 cm s^{-1}. Therefore, the terminal settling
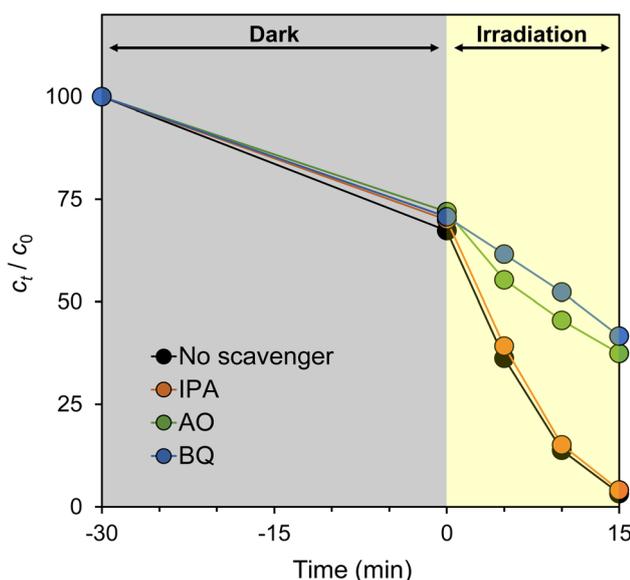

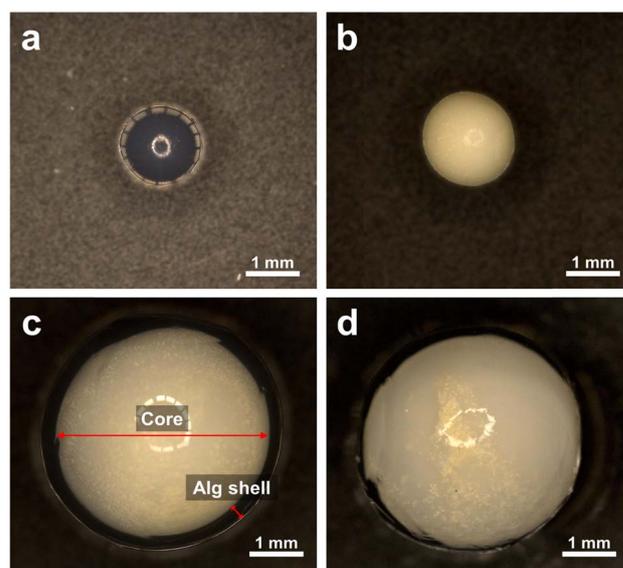**Fig. 7** Active species trapping experiment using different scavengers.

Fig. 8 Microscopic images of (a) a Alg bead, (b) a g-C$_3$N$_4$/Alg bead, (c) a g-C$_3$N$_4$/Alg capsule and (d) agglomeration of g-C$_3$N$_4$ in the capsule.

velocity of g-C$_3$N$_4$/Alg beads is at least 12 times faster than that of the powder. At this velocity, in the separation process after pollutant degradation, the g-C$_3$N$_4$/Alg beads can be easily separated from treated water in a very short period of standing time. Whilst since 1.2 μm is merely the average particle diameter of powdered g-C$_3$N$_4$ and much smaller size particles are also included, it requires centrifugation with 13 000 rpm for 30 min to separate them from the media completely. These results demonstrate that immobilization of g-C$_3$N$_4$ in alginate beads improves recovery.

Fig. 9 summarizes the photocatalytic activity of powdered CN-TU, CN-TU immobilized in Alg beads (g-C$_3$N$_4$/Alg beads), and CN-TU immobilized in Alg capsules (g-C$_3$N$_4$/Alg capsules). A control experiment using Alg beads not containing g-C$_3$N$_4$ demonstrated a negligible decrease in RhB concentration, suggesting RhB is stable under visible light irradiation and that the alginate hydrogel negligibly adsorbs RhB. Therefore, the decrease in RhB concentration may be attributed to photocatalytic degradation in the experiments involving g-C$_3$N$_4$/Alg beads and g-C$_3$N$_4$/Alg capsules. As expected, the degradation rate of immobilized g-C$_3$N$_4$ was inferior to the powder because RhB diffusion is hindered inside the alginate hydrogel. Comparing the two types of immobilization methods, g-C$_3$N$_4$/Alg beads completely decolorized RhB (10 ppm) in 60 min, whereas g-C$_3$N$_4$/Alg capsules decolorized only 60%. Photocatalytic activities of the g-C$_3$N$_4$/Alg beads and capsules were evaluated by a first-order kinetic constant, and were 0.049 and 0.012 min^{-1}, respectively. The photocatalytic activity of the g-C$_3$N$_4$/Alg beads is approximately 4 times higher than that of the g-C$_3$N$_4$/Alg capsules. The capsules seemed to have a lower mass transfer resistance than the beads because the alginate layer is thinner for the g-C$_3$N$_4$/Alg capsules than for the g-C$_3$N$_4$/Alg beads (shell thickness, 0.3 mm; bead radius, 1.2 mm). However, increased mass transfer resistance in the capsule may originate from their larger diameters (4.42 mm, vs. 2.43 mm for beads)
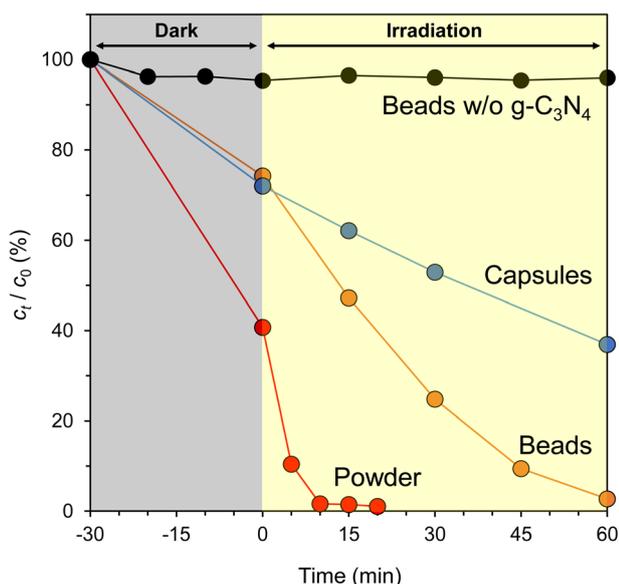

Fig. 9 RhB degradation by two types of g-C$_3$N$_4$/Alg hydrogel spheres.

and highly viscous, PVP solution-filled cores. Furthermore, Fig. 8d shows an example of agglomeration of g-C$_3$N$_4$ particles inside a capsule sample; this was observed in some but not all capsule samples. Thus, decreased contact area with RhB could decrease photocatalytic activity of g-C$_3$N$_4$/Alg capsules. In contrast, the g-C$_3$N$_4$/Alg beads showed higher photocatalytic activity because the immobilized particles did not agglomerate. These results confirmed that solid alginate hydrogel beads are more suitable as carriers for the immobilization of g-C$_3$N$_4$. In previous studies in which g-C$_3$N$_4$ was immobilized in alginate hydrogels, even under optimal conditions, the degradation of RhB (10 ppm) took 3–36 h.[33,34] Neither study formed heterojunctions in g-C$_3$N$_4$, which did not improve the charge separation problem. Hao et al. added a higher concentration of g-C$_3$N$_4$ (15% w/v) to the alginate solution,[36] which would have resulted in a higher photocatalyst content per bead and poor light penetration inside the beads. This means that the self-shading effect of the photocatalyst could decrease in photocatalytic activity. Falletta et al. had a larger bead diameter (5 mm),[37] which could decrease diffusion rate of the RhB solution. In contrast, isotype heterojunction g-C$_3$N$_4$ with improved charge separation were immobilized at a low concentration (1% w/v) in alginate beads with smaller diameter (2.43 mm) in this study, suggesting high activity of g-C$_3$N$_4$ itself, high light penetration, and low mass transfer resistance may explain our improved photocatalytic performance. In addition, both previous studies were carried out using xenon lamp irradiation without eliminating the UV light range in their experiments. Nonetheless, the g-C$_3$N$_4$/Alg beads in this study demonstrated improved photocatalytic activity, as evidenced by the complete decolorization of RhB (10 ppm) in 60 min using only visible light.

3.5. Recycling tests of g-C$_3$N$_4$/Alg beads

Recycling tests were performed to prove the practicality of the g-C$_3$N$_4$/Alg beads. Fig. 10a shows changes of RhB concentration over time during exposure to visible-light irradiation, and Fig. 10b shows the photocatalytic activity of g-C$_3$N$_4$/Alg beads during 10 repeated degradation cycles. Interestingly, the photocatalytic activity improved in the 2nd run; in the subsequent runs, RhB was completely decolorized within 45 min. This enhancement could originate from slight photocatalytic degradation of the carrier alginate hydrogel, resulting in pore widening or channel formation that facilitated improved RhB diffusion rate inside the beads.[44] As shown in the FE-SEM images (Fig. 11a and b), the surface of the beads immediately after synthesis was smooth (Fig. 11a), whereas wrinkles were observed on the surface of the beads after recycling (Fig. 11b). This observation suggests that the degradation of the alginate hydrogel inside the beads created a slight cavity that caused nonuniform shrinkage during drying. Moreover, the consistent photocatalytic activity throughout the 10 repeated cycles suggests that the g-C$_3$N$_4$ particles did not leak from the beads. This represents an improvement from previous studies using N,N-dimethylacrylamide or chitosan hydrogels as carriers, which demonstrated decreased degradation rates over the course of recycling experiments. Those materials may have
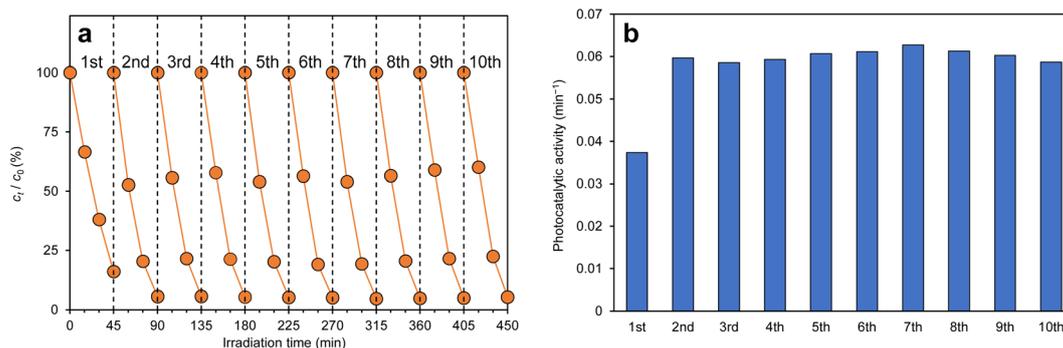
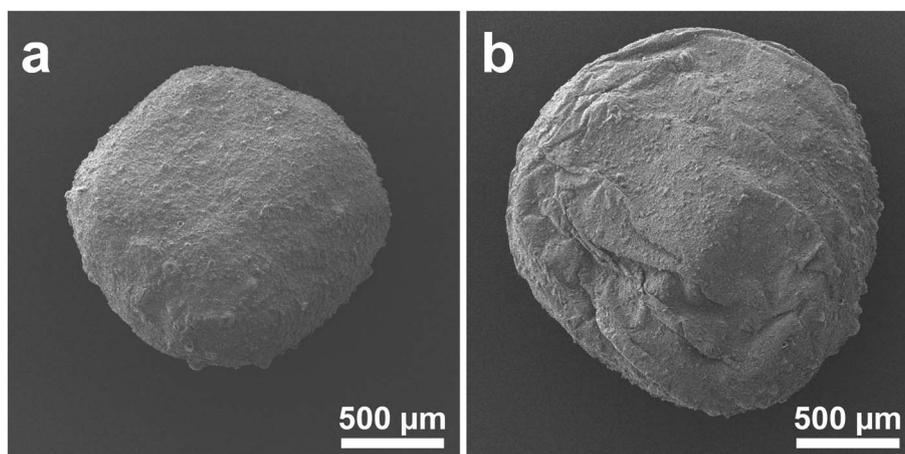**Fig. 10** (a)Temporal changes in RhB concentration and (b) photocatalytic activity in recycling tests of g-C_3N_4/Alg beads.

Fig. 11 SEM images of g-C_3N_4/Alg bead (a) before and (b) after 10 repeated degradation experiments.

insufficiently cross-linked in the presence of photocatalytic particles, leading to gel collapse and photocatalytic particle loss following repeated degradation experiments.[45,46]

Furthermore, the durability of g-C_3N_4/Alg beads was evaluated during the 10 repeated cycles. Fig. S1† shows the bead elastic modulus with respect to irradiation time following each cycle. The g-C_3N_4/Alg beads maintained a constant elastic modulus throughout the 10 cycles despite demonstrating activity for RhB degradation. The original bead strength could be further improved by adding poly(vinyl alcohol) (PVA), a biodegradable polymer, to the precursor material. Li *et al.* developed a PVA/alginate hydrogel with up to four times the elastic modulus relative to a simple alginate hydrogel.[47] These results prove that the g-C_3N_4/Alg beads developed in this study are sufficiently durable and are useful photocatalysts that overcome previous difficulties involving recovery and reuse.

4. Conclusions

In this study, we demonstrated facile syntheses of isotype heterojunction g-C_3N_4 using a ball mill. g-C_3N_4 synthesized from urea and thiourea showed the highest photocatalytic activity owing to high specific surface area and effective charge separation. The results of the active species trapping experiments suggest that $^•O_2^-$ and holes, rather than $^•OH$, contribute to RhB degradation. Moreover, the isotype heterojunction g-C_3N_4 was immobilized in alginate hydrogel spheres. A comparison of the bead shapes and hollow capsules showed that the g-C_3N_4/Alg beads with well-dispersed g-C_3N_4 particles exhibited better photocatalytic activity. Repeated RhB degradation experiments using g-C_3N_4/Alg beads showed no decrease in photocatalytic activity, and the beads maintained their elastic moduli throughout the entire cycle. This study demonstrates the synthesis of recyclable isotype heterojunction g-C_3N_4 that may circumvent present challenges to the practical application of sustainable photocatalytic wastewater treatment.

Data availability

The data supporting this article have been included as part of the ESI.†

Conflicts of interest

The authors declare that they have no known competing financial interests or personal relationships that could have appeared to influence the work reported in this paper.

Acknowledgements

References

1 L. Ding, S. Yang, Z. Liang, X. Qian, X. Chen, H. Cui and J. Tian, TiO$_2$ nanobelts with anatase/rutile heterophase junctions for highly efficient photocatalytic overall water splitting, *J. Colloid Interface Sci.*, 2020, **567**, 181–189, DOI: 10.1016/j.jcis.2020.02.014.

2 Y. Li, M. Zhou, B. Cheng and Y. Shao, Recent advances in g-C$_3$N$_4$-based heterojunction photocatalysts, *J. Mater. Sci. Technol.*, 2020, **56**, 1–17, DOI: 10.1016/j.jmst.2020.04.028.

3 E. T. Wahyuni, T. Rahmaniati, A. R. Hafidzah, S. Suherman and A. Suratman, Photocatalysis over N-doped TiO$_2$ driven by visible light for Pb(II) removal from aqueous media, *Catalysts*, 2021, **11**(8), 945, DOI: 10.3390/catal11080945.

4 S. Cravanzola, F. Cesano, F. Gaziano and D. Scarano, Sulfur-doped TiO$_2$: structure and surface properties, *Catalysts*, 2017, **7**(7), 214, DOI: 10.3390/catal7070214.

5 H. Irie, S. Miura, K. Kamiya and K. Hashimoto, Efficient visible light-sensitive photocatalysts: grafting Cu(II) ions onto TiO$_2$ and WO$_3$ photocatalysts, *Chem. Phys. Lett.*, 2008, **457**, 202–205, DOI: 10.1016/j.cplett.2008.04.006.

6 R. Nakamura, A. Okamoto, H. Osawa, H. Irie and K. Hashimoto, Design of all-inorganic molecular-based photocatalysts sensitive to visible light: Ti(IV)-O-Ce(III) bimetallic assemblies on mesoporous silica, *J. Am. Chem. Soc.*, 2007, **129**, 9596–9597, DOI: 10.1021/ja073668n.

7 H. Yu, H. Irie, Y. Shimodaira, Y. Hosogi, Y. Kuroda, M. Miyauchi and K. Hashimoto, An efficient visible-light-sensitive Fe(III)-grafted TiO$_2$ photocatalyst, *J. Phys. Chem. C*, 2010, **114**, 16481–16487, DOI: 10.1021/jp1071956.

8 M. Ghosh, P. Chowdhury and A. K. Ray, Photocatalytic activity of aeroxide TiO$_2$ sensitized by natural dye extracted from mangosteen peel, *Catalysts*, 2020, **10**(8), 917, DOI: 10.3390/catal10080917.

9 S. Goulart, L. J. J. Nieves, A. G. D. Bó and A. M. Bernardin, Sensitization of TiO$_2$ nanoparticles with natural dyes extracts for photocatalytic activity under visible light, *Dyes Pigm.*, 2020, **182**(3), 108654, DOI: 10.1016/j.dyepig.2020.108654.

10 M. Liao, L. Su, Y. Deng, S. Xiong, R. Tang, Z. Wu, C. Ding, L. Yang and D. Gong, Strategies to improve WO$_3$-based photocatalysts for wastewater treatment: a review, *J. Mater. Sci.*, 2021, **56**, 14416–14447, DOI: 10.1007/s10853-021-06202-8.

11 Y. Cui, M. Li, N. Zhu, Y. Cheng, S. S. Lam, J. Chen, Y. Gao and J. Zhao, Bi-based visible light-driven nano-photocatalyst: the design, synthesis, and its application in pollutant governance and energy development, *Nano Today*, 2022, **43**, 101432, DOI: 10.1016/j.nantod.2022.101432.

12 W. J. Ong, L. L. Tan, Y. H. Ng, S. T. Yong and S. P. Chai, Graphitic carbon nitride (g-C$_3$N$_4$)-based photocatalysts for artificial photosynthesis and environmental remediation:

13 L. Shi, K. Chang, H. Zhang, X. Hai, L. Yang, T. Wang and J. Ye, Drastic Enhancement of Photocatalytic Activities over Phosphoric Acid Protonated Porous g-C$_3$N$_4$ Nanosheets under Visible Light, *Small*, 2016, 4431–4439, DOI: 10.1002/smll.201601668.

14 K. Cerdan, W. Ouyang, J. C. Colmenares, M. J. Muñoz-Batista, R. Luque and A. M. Balu, Facile mechanochemical modification of g-C$_3$N$_4$ for selective photo-oxidation of benzyl alcohol, *Chem. Eng. Sci.*, 2019, **194**, 78–84, DOI: 10.1016/j.ces.2018.04.001.

15 Y. Li, R. Jin, Y. Xing, J. Li, S. Song, X. Liu, M. Li and R. Jin, Macroscopic foam-like holey ultrathin g-C$_3$N$_4$ nanosheets for drastic improvement of visible-light photocatalytic activity, *Adv. Energy Mater.*, 2016, **6**, 1601273, DOI: 10.1002/aenm.201601273.

16 H. Niu, W. Zhao, H. Lv, Y. Yang and Y. Cai, Accurate design of hollow/tubular porous g-C$_3$N$_4$ from melamine-cyanuric acid supramolecular prepared with mechanochemical method, *Chem. Eng. J.*, 2021, **411**, 128400, DOI: 10.1016/j.cej.2020.128400.

17 H. Zhang, C. Zhu, J. Cao, Q. Tang, M. Li, P. Kang, C. Shi and M. Ma, Ultrasonic-assisted synthesis of 2D α-Fe$_2$O$_3$@g-C$_3$N$_4$ composite with excellent visible light photocatalytic activity, *Catalysts*, 2018, **8**, 457, DOI: 10.3390/catal8100457.

18 Y. Yang, J. Zhu, Y. He, M. Li, Y. Liu, M. Chen and D. Cao, Charge transfer in photocatalysis of direct Z-scheme g-C$_3$N$_4$-based ferroelectric heterojunction, *J. Alloys Compd.*, 2022, **893**, 162270, DOI: 10.1016/j.jallcom.2021.162270.

19 J. Hongxia, G. Yanlin, L. Longxiang, W. Xu and P. Wangjun, A new double Z-scheme TiO$_2$/ZnO-g-C$_3$N$_4$ nanocomposite with enhanced photodegradation efficiency for Rhodamine B under sunlight, *Environ. Prog. Sustainable Energy*, 2022, e13968, DOI: 10.1002/ep.13968.

20 J. Lin, W. Tian, H. Zhang, X. Duan, H. Sun, H. Wang, Y. Fang, Y. Huang and S. Wang, Carbon nitride-based Z-scheme heterojunctions for solar-driven advanced oxidation processes, *J. Hazard. Mater.*, 2022, **434**, 128866, DOI: 10.1016/j.jhazmat.2022.128866.

21 M. Solehudin, U. Sirimahachai, G. A. M. Ali, K. F. Chong and S. Wongnawa, One-pot synthesis of isotype heterojunction g-C$_3$N$_4$-MU photocatalyst for effective tetracycline hydrochloride antibiotic and reactive orange 16 dye removal, *Adv. Powder Technol.*, 2020, **31**, 1891–1902, DOI: 10.1016/j.apt.2020.02.020.

22 G. Liao and W. Yao, Facile synthesis of porous isotype heterojunction g-C$_3$N$_4$ for enhanced photocatalytic degradation of RhB under visible light, *Diamond Relat. Mater.*, 2022, **128**, 109227, DOI: 10.1016/j.diamond.2022.109227.

23 A. Balakrishnan, E. S. Kunnel, R. Sasidharan, M. Chinthala and A. Kumar, 3D black g-C$_3$N$_4$ isotype heterojunction hydrogels as a sustainable photocatalyst for tetracycline degradation and H$_2$O$_2$ production, *Chem. Eng. J.*, 2023, **475**, 146163, DOI: 10.1016/j.cej.2023.146163.

24 F. Dong, Z. Zhao, T. Xiong, Z. Ni, W. Zhang, Y. Sun and W. K. Ho, In situ construction of g-C₃N₄/g-C₃N₄ metal-free heterojunction for enhanced visible-light photocatalysis, *ACS Appl. Mater. Interfaces*, 2013, **5**, 11392–11401, DOI: **10.1021/am403653a**.

25 A. Balakrishnan, K. V. Suryaa, H. Tripathy, S. Trivedi, A. Kumar and M. Chinthala, Phosphorylated g-C₃N₄/sulfur self-doped g-C₃N₄ homojunction carboxymethyl cellulose beads: an efficient photocatalyst for H₂O₂ production, *J. Colloid Interface Sci.*, 2024, **663**, 1087–1098, DOI: **10.1016/j.jcis.2024.02.110**.

26 D. P. MacWan, P. N. Dave and S. Chaturvedi, A review on nano-TiO₂ sol-gel type syntheses and its applications, *J. Mater. Sci.*, 2011, **46**, 3669–3686, DOI: **10.1007/s10853-011-5378-y**.

27 G. D. Shen, Y. P. Pu, Y. F. Cui and P. P. Jing, Easy synthesis of TiO₂/g-C₃N₄ heterostructure photocatalyst with large surface area and excellent photocatalytic activity, *Ceram. Int.*, 2017, **43**, S664–S670, DOI: **10.1016/j.ceramint.2017.05.243**.

28 N. Jan, N. Majeed, M. Ahmad, W. A. Lone and R. John, Nano-pollution: why it should worry us, *Chemosphere*, 2022, **302**, 134746, DOI: **10.1016/j.chemosphere.2022.134746**.

29 H. P. S. A. Khalil, C. K. Saurabh, Y. Y. Tye, T. K. Lai, A. M. Easa, E. Rosamah, M. R. N. Fazita, M. I. Syakir, A. S. Adnan, H. M. Fizree, N. A. S. Aprilia and A. Banerjee, Seaweed based sustainable films and composites for food and pharmaceutical applications: a review, *Renewable Sustainable Energy Rev.*, 2017, **77**, 353–362, DOI: **10.1016/j.rser.2017.04.025**.

30 F. Abasalizadeh, S. V. Moghaddam, E. Alizadeh, E. Akbari, E. Kashani, S. M. B. Fazljou, M. Torbati and A. Akbarzadeh, Alginate-based hydrogels as drug delivery vehicles in cancer treatment and their applications in wound dressing and 3D bioprinting, *J. Biol. Eng.*, 2020, **14**, 8, DOI: **10.1186/s13036-020-0227-7**.

31 M. T. ALSamman and J. Sánchez, Recent advances on hydrogels based on chitosan and alginate for the adsorption of dyes and metal ions from water, *Arabian J. Chem.*, 2021, **14**, 103455, DOI: **10.1016/j.arabjc.2021.103455**.

32 Z. Tian, L. Zhang, X. Sang, G. Shi and C. Ni, Preparation and flocculation performance study of a novel amphoteric alginate flocculant, *J. Phys. Chem. Solids*, 2020, **141**, 109408, DOI: **10.1016/j.jpcs.2020.109408**.

33 F. Kurayama, N. Mohammed Bahadur, T. Furusawa, M. Sato and N. Suzuki, Facile preparation of aminosilane-alginate hybrid beads for enzyme immobilization: kinetics and equilibrium studies, *Int. J. Biol. Macromol.*, 2020, **150**, 1203–1212, DOI: **10.1016/j.ijbiomac.2019.10.130**.

34 F. Kurayama, N. M. Bahadur, M. Sato, T. Furusawa and N. Suzuki, One-step preparation of organic-inorganic hybrid capsules based on simultaneous gelation and silicification, *Eng. Rep.*, 2019, **1**, e12061, DOI: **10.1002/eng2.12061**.

35 A. Balakrishnan and M. Chinthala, Comprehensive review on advanced reusability of g-C₃N₄ based photocatalysts for the removal of organic pollutants, *Chemosphere*, 2022, **297**, 134190, DOI: **10.1016/j.chemosphere.2022.134190**.

36 D. Hao, Q. Huang, W. Wei, X. Bai and B. J. Ni, A reusable, separation-free and biodegradable calcium alginate/g-C₃N₄ microsphere for sustainable photocatalytic wastewater treatment, *J. Cleaner Prod.*, 2021, **314**, 128033, DOI: **10.1016/j.jclepro.2021.128033**.

37 E. Falletta, M. Longhi, A. di Michele, D. C. Boffito and C. L. Bianchi, Floatable graphitic carbon nitride/alginate beads for the photodegradation of organic pollutants under solar light irradiation, *J. Cleaner Prod.*, 2022, **371**, 133641, DOI: **10.1016/j.jclepro.2022.133641**.

38 F. Dong, Z. Wang, Y. Sun, W. K. Ho and H. Zhang, Engineering the nanoarchitecture and texture of polymeric carbon nitride semiconductor for enhanced visible light photocatalytic activity, *J. Colloid Interface Sci.*, 2013, **401**, 70–79, DOI: **10.1016/j.jcis.2013.03.034**.

39 Y. Zheng, Z. Zhang and C. Li, A comparison of graphitic carbon nitrides synthesized from different precursors through pyrolysis, *J. Photochem. Photobiol., A*, 2017, **332**, 32–44, DOI: **10.1016/j.jphotochem.2016.08.005**.

40 B. Zhu, P. Xia, W. Ho and J. Yu, Isoelectric point and adsorption activity of porous g-C₃N₄, *Appl. Surf. Sci.*, 2015, **344**, 188–195, DOI: **10.1016/j.apsusc.2015.03.086**.

41 J. Zhang, X. Chen, K. Takanabe, K. Maeda, K. Domen, J. D. Epping, X. Fu, M. Antonieta and X. Wang, Synthesis of a carbon nitride structure for visible-light catalysis by copolymerization, *Angew. Chem., Int. Ed.*, 2010, **49**, 441–444, DOI: **10.1002/anie.200903886**.

42 T. K. A. Nguyen, T. T. Pham, H. Nguyen-Phu and E. W. Shin, The effect of graphitic carbon nitride precursors on the photocatalytic dye degradation of water-dispersible graphitic carbon nitride photocatalysts, *Appl. Surf. Sci.*, 2021, **537**, 148027, DOI: **10.1016/j.apsusc.2020.148027**.

43 S. Dong, Z. Zeng, W. Cai, Z. Zhou, C. Dou, H. Liu and J. Xia, The zeta potentials of g-C₃N₄ nanoparticles: effect of electrolyte, ionic strength, pH, and humic acid, *J. Nanopart. Res.*, 2019, **21**, 233, DOI: **10.1007/s11051-019-4686-z**.

44 D. Xiong, W. Zhao, J. Guo, S. Li, Y. Ye, L. E and X. Yang, Highly efficient and reusable BiOCl photocatalyst modulating by hydrogel immobilization and oxygen vacancies engineering, *Sep. Purif. Technol.*, 2021, **277**, 119628, DOI: **10.1016/j.seppur.2021.119628**.

45 Q. Cao, J. Barrio, M. Antonietti, B. Kumru, M. Shalom and B. V. K. J. Schmidt, Photoactive graphitic carbon nitride-based gel beads as recyclable photocatalysts, *ACS Appl. Polym. Mater.*, 2020, **2**, 3346–3354, DOI: **10.1021/acsapm.0c00453**.

46 C. Zhao, Q. Yan, S. Wang, P. Dong and L. Zhang, Regenerable g-C₃N₄-chitosan beads with enhanced photocatalytic activity and stability, *RSC Adv.*, 2018, **8**, 27516–27524, DOI: **10.1039/c8ra04293d**.

47 X. Li, M. Shu, H. Li, X. Gao, S. Long, T. Hu and C. Wu, Strong, tough and mechanically self-recoverable poly(vinyl alcohol)/alginate dual-physical double-network hydrogels with large cross-link density contrast, *RSC Adv.*, 2018, **8**, 16674–16689, DOI: **10.1039/c8ra01302k**.